POLITECNICO DI TORINO

Master's Degree in Energy and Nuclear Engineering

Master's Degree Thesis

Mechanical characterization of Fe-10Cr-4Al micro-samples for ion irradiation testing application

Supervisors
Prof. Monica Ferraris
Prof. Pär Olsson

Candidate
Andrea Celi

Marzo 2024

Acknowledgements

I would like to take this opportunity to express my gratitude to all those who have contributed to the realization of this thesis. Firstly, I would like to thank my supervisor at Politecnico di Torino, Monica Ferraris, for giving me this opportunity and for her continued encouragement even from afar. I would also like to thank my supervisor at KTH Royal Institute of Technology, Pär Olsson for the trust he showed to me, his commitment and support. Special thanks to Faris Sweidan for patience, guidance, and support which have pushed me forward with this thesis. I am also immensely grateful to Christopher Petersson for his availability, and for the time dedicated to me and this thesis. His knowledge and feedback were fundamental for the completion of this project. Finally, I would like to extend my gratitude to Michela, for being always with me, giving constant support and always believing in me, especially in my darkest hours. I would like to thank my family and my friends for having always supported and believed in my choices.

Abstract

One of the most promising structural materials for lead-cooled fast reactors is ferritic FeCrAl steel due to the high temperature oxidation resistance, corrosion resistance and also radiation-induced swelling resistance. FeCrAl steels have also shown very good resistance to liquid metal embrittlement but what effect irradiation have on this phenomenon is still not well-known. The use of proton irradiation in nuclear materials science to simulate the damage of neutron irradiation has been widely explained. Despite the use of proton irradiation in nuclear materials science to simulate the damage of neutron irradiation on materials has been encouraged by numerous studies, ions have the disadvantages to present a very limited penetration depth resulting in radiation damage limited to the surface layer in standard size FeCrAl samples. This thesis analyses an alternative option by focusing on the micro-sizing of the samples so that they are not subjected to radiation damage only on the surface. The aim of this work is to test a possible minimal dimension of samples in order to find a comparable mechanical response to the standard metallic behaviour. The samples were tested with a slow strain rate testing rig at room temperature, $250°C$, $350°C$, $400°C$ and $450°C$ in air, in a gas mixture of Ar-5% H2 and in liquid lead. The results showed that FeCrAl micro-sample mechanical representation could be compared to standard samples values already present in literature for what concerned lower temperature, while high temperature test showed lack of consistency.

Keywords

FeCrAl, ion irradiation, lead-cooled fast reactor, micro-sizing, Slow Strain Rate Testing rig.

Acronyms

BWR Boling Water Reactor
DBTT Ductile to Brittle Transition Temperature
EDS energy dispersion spectroscopy
GEN IV Generation IV
KTH Kungliga Tekniska högskolan
LBE Lead-Bismuth Eutectic
LFR Lead-cooled Fast Reactor
LWR Light Water Reactor
PWR Pressurized Water Reactor
RE Reactive Elements
SIA Self-Interstitial Atoms
SEM Scanning Electron Microscope
SSRT Slow Strain Rate Testing
UTS Ultimate tensile strength
YS Yield strength

List of Figures

List of Tables

Contents

Chapter 1

Introduction

The ever-increasing energy demand due to growing world population and growing economies of developing nations is one of the world's main problems nowadays. In 2022 over 80% of primary energy consumption in the world and over 60% of its electricity was from fossil fuels, resulting in a negative impact on environment being the fossil fuel consumption the largest driver of global climate change due to remarkable amount of greenhouse gas emission and the main contributor to water, soil and air pollution, which is estimated to be linked to millions of premature deaths each year [1] [2]. In addition fossil fuels are classified as non-renewable resources because known reserves are being exhausted much faster than new ones are replenished [3].

Therefore, the necessity for secure and long-term solutions arise and the aim to shift from fossil fuel energy to sustainable energy sources to meet carbon neutrality goal, lead to the nuclear energy to be taken into account.

1.1 Lead-cooled fast reactors

The majority of reactors currently in operation in the world are II and III generation reactor systems. Generation IV reactors are nuclear reactors under development since 2000, whose designs are intended to represent the future of nuclear energy [4].

Generation IV reactors should meet definite goals, involving sustainability, economics, safety and reliability, proliferation resistance and physical protection. In terms of sustainability, they should provide sustainable energy generation that meets clean air objectives, guarantees long-term availability of systems, maximizes fuel utilisation, minimises nuclear waste, leading to an improving protection for people and environment. In terms of economics they should guarantee a life-cycle cost advantage and a similar level of financial risk as compared to other energy sources. Moreover they should provide exceptional standards in terms of safety and reliability resulting in an almost nonexistent likelihood of core damage and non-necessity of offsite emergency response. Lastly, in terms of proliferation resistance and physical protection, they should represent an unappealing choice for diversion or theft of weapons-usable materials [5] [6].

Among the six designs chosen to be revolutionaries because of their discontinuity with generation II and III reactors, the Lead-cooled Fast Reactor (LFR) seems to offer the best

combination of characteristics and advantages [7]. LFRs fuel sustainability is increased by the conversion capability of closed fuel cycle and due to the fast-neutron spectrum working window as well as high temperature operation they can also be used as a burner to consume actinides from spent light-water reactor fuel. The enhanced safety is provided by the non-dependence on diesel generators backup power in case of blackout conditions due to the passive decay heat removal enabled by the natural circulation of liquid lead coolant, and the impossibility of a loss of primary coolant even in the case of a failure of the reactor vessel due to its optimized design [8]. The implementation of molten lead as a relatively inert and low-pressure coolant makes LFR one of the most promising among Generation IV reactors, due to the enhanced safety and proliferation resistance, design simplification, sustainability and consequential economic competitiveness. In fact, as a dense liquid lead shows excellent cooling properties while due to the low tendency to absorb or slow down neutrons provide the possibility to sustain the high neutron energies needed in a fast reactor [8]. Thus, due to the high margin to boiling and the relatively chemical inertness of liquid lead, the issues linked to coolant boiling are minimized and the occurrence of rapid chemical interactions with air and water and hydrogen generation that can conduct to considerable energy release is eliminated. This represent a substantial improvement in terms of safety, as well as an opportunity in plant simplification avoiding contemporaneous control of temperature, pressure and coolant level [9].

On the other hand, the presence of liquid lead as coolant entails many challenges that are currently under consideration and research. Thermo-mechanical properties of lead as its high melting point and density, opacity and strong corrosion tendency represent issue that have to be faced [8].

The high melting temperature requires that the primary coolant system has to be maintained at temperatures to prevent the solidification of the lead coolant or at least to maintain a recirculation at core level to allow its cooling. The high density presents challenges in terms of structural design to avoid seismic impacts to the reactor, while the lead opacity results in the need of careful operations during inspection and monitoring of reactor in-core components and fuel handling. Beyond these surmountable issues, the most significant challenges result from the tendency of lead at high temperatures to be corrosive when in contact with structural steels [8]. In the recent years FeCrAl alloy emerged as a plausible solution for structural materials to be used in lead and lead−bismuth cooled nuclear applications due to the high temperature oxidation resistance, corrosion resistance and stress corrosion cracking resistance and also radiation-induced swelling resistance [10] [11].

1.2 Aim

The idea behind this thesis is to contribute in the mechanical characterization of FeCrAl alloy, given its promising characteristic in the nuclear field. FeCrAl steels have shown very good resistance to liquid metal embrittlement but which effects irradiation have on this phenomenon is still not well-known. Despite the use of proton irradiation in nuclear materials science to simulate the damage of neutron irradiation on materials has been encouraged by numerous studies, ions have the disadvantages to present a very limited

penetration depth resulting in radiation damage limited to the surface layer in standard size FeCrAl samples. The thesis analyses an alternative option by focusing on the micro-sizing of the samples for future irradiation study applications. The micro-sized samples advantage is that they are not subjected to radiation damage only on the surface, allowing to obtain an optimized analysis of the mechanical behaviour of the irradiated FeCrAl. The aim of this work is to test a possible minimal dimension of samples in order to find a comparable mechanical response to the standard metallic behaviour.

1.3 Stakeholders

There are two primary stakeholders in the project:

- The supervisor at KTH - Royal Institute of Technology
- The supervisor at Politecnico di Torino

1.4 Outline

Chapter 2 of this thesis will deal with all relevant theoretical background to the project with a main focus on FeCrAl material. Chapter 3 will explain the experimental procedure carried out for this project. The results and discussion will be addressed in Chapter 4. Chapter 5 will report the conclusions of the project, including suggestions for future work.

Chapter 2

Theoretical background

2.1 FeCrAl

In the last decades an increasing amount of research has been focused on the development of FeCrAl alloys for nuclear applications. FeCrAl alloys are currently studied for nuclear applications mainly due to the high temperature oxidation resistance, corrosion resistance and stress corrosion cracking resistance and also radiation-induced swelling resistance [10].

2.1.1 High temperature oxidation resistance

The high temperature oxidation resistance shown by FeCrAl alloys is related to the formation of a α-Al_2O_3 (alumina) layer on the exposed surfaces due to preferential oxidation of Al inside the alloy. The layer is adherent to the surface after quenching, increasing resistance to oxidation. The Cr content is helpful regarding the layer scale formation. Under highly oxidizing environments characteristic of LWR severe accidents, the FeCrAl class of ferritic alloys offers oxidation rates roughly three orders of magnitude slower than Zr-based alloys. As result, the coping time rise to approximately 3200 s, respect to 1200 s for Zr-based alloys in similar situation [10] [12].

2.1.2 Corrosion resistance

Studies carried out in pressurized water reactor (PWR) and boiling water reactor (BWR) under low and high oxygen activity show high temperature and high pressure hydrothermal corrosion resistance. The results of the immersion tests indicate a thickness loss for FeCrAl alloys after one year of corrosion around $\sim 2\mu m$ or less, comparable to Zirclaoy-4 at similar temperatures, and actually negligible [13].

2.1.3 Stress corrosion cracking resistance

Since FeCrAl alloys have never been used in LWR, not enough data was present to establish if stress corrosion cracking (SCC) is a concern for FeCrAl alloys. Current data show that the presence of 5% to 6% of Al in the FeCrAl alloys makes them as resistant to SCC at high temperature as the Fe-Cr alloys. FeCrAl alloys may only suffer SCC at

high levels of applied stress intensity, which should not be a concern in any of reactor condition [14].

2.1.4 Radiation induced swelling resistance

FeCrAl alloys show an higher radiation induced swelling resistance compared to Zr-based alloys. As it was well know for high-Cr ferritic alloys, FeCrAl alloys show no presence of voids or cavities in the microstructure at dpa rates typically used in fuel applications [15].

2.2 Fe-10Cr-4Al

Mechanical properties of ferritic FeCrAl alloys are a function of temperature, composition and microstructure. Additions of Cr and Al are essential for improving oxidation resistance at elevated temperatures by forming the alumina layer on the surface. The effect of oxidation resistance increases with the amounts of Cr and Al additions. The Cr addition is also known to reduce the required amount of the Al addition to form aluminum oxide scale. To develop FeCrAl alloys with lower Cr content due to radiation embrittlement process an Al content $\geq 5\%$ is required to form the alumina layer, resulting in a decreasing in fabricability and ductility [10] [16].

As it is shown in Figure 2.1 yield strength and total elongation depend on Cr and Al content. Yield strength increases at a rate of 35 MPa/wt.% Al with a decrease in total elongation. Higher Al content increases the deformation resistance and so lowers the fabricability of the alloy. Low Cr alloys show little variation in hardness while high Cr alloys show significant increases in hardness with time.

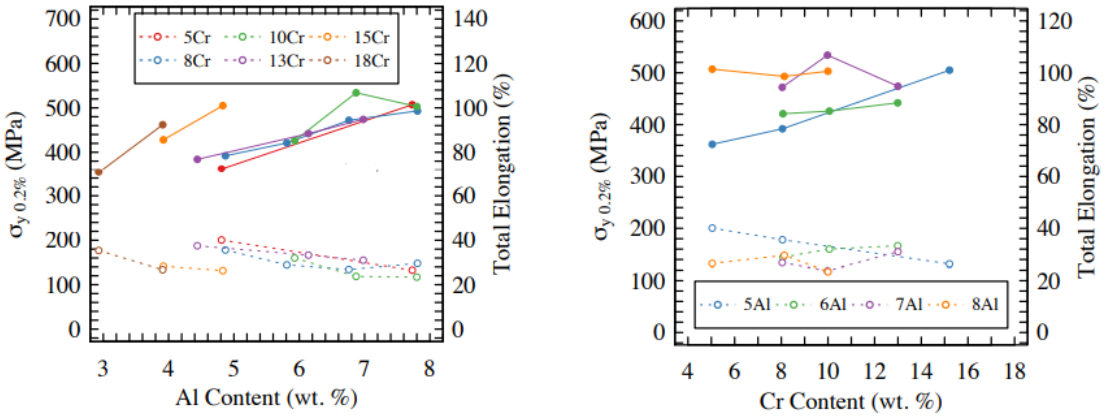

Figure 2.1. Room temperature tensile properties of model FeCrAl alloys as a function of Al content and Cr content. Reproduced from *Handbook on the material properties of FeCrAl alloys for nuclear power production applications.*

Figure 2.2 shows the effect of Al on the ductile to brittle transition temperature (DBTT) in high Cr content FeCrAl alloys. Increasing Al content from $3wt.\%$ to $6wt.\%$

leads to a $100 - 150°C$ increase in the DBTT. The influence of Al on the ductile behavior of FeCrAl alloys reduces the fabricability of higher Al content FeCrAl alloys. While, Cr amount shows limited effect on the transition temperature, even for higher Cr content (23-25 wt.% Cr) [17] [10].

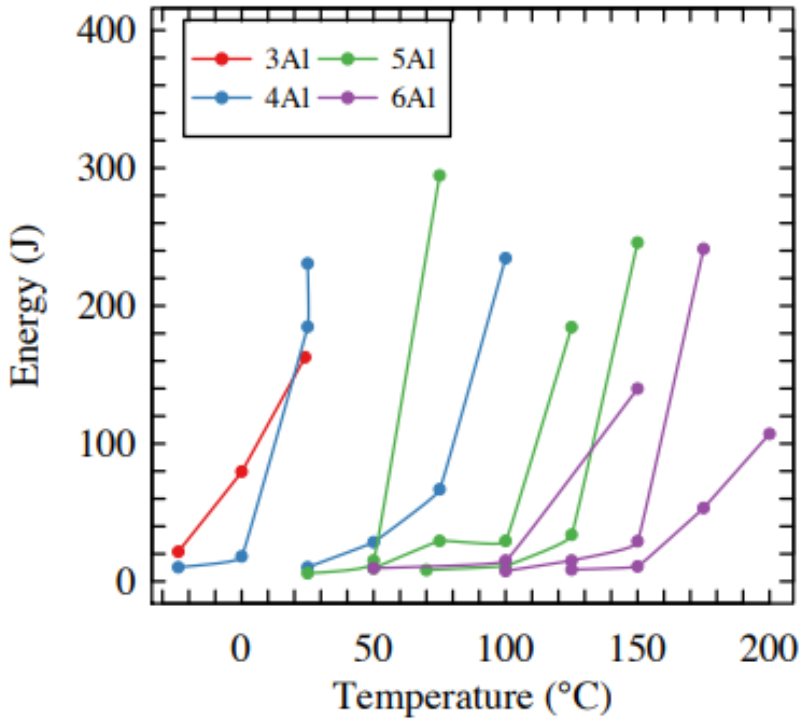

Figure 2.2. Ductile to brittle transition temperature as a function of Al content in high content Cr FeCrAl alloys. Reproduced from *Handbook on the material properties of FeCrAl alloys for nuclear power production applications.*

Reactive element additions have shown to reduce the growth rate of the alumina scale and increase the adherence of the alumina layer during oxidation, resulting in an improvement in corrosion resistance and in its mechanical properties [18]. The material used in this work is a Fe-10Cr-4Al alloy, developed by KTH together with Sandvik and Kanthal [18] [19]. The RE additions have been optimized for high temperature lead and lower oxygen tests, due to due to the optimised RE/C-ratio, as RE effect is resulting in precipitates formation at the metal-oxide interface. These precipitates advantage the formation of protective oxides on the surface and increase the oxide adhesion. The Ti additions show promising contribution to the oxidation properties of Fe-10Cr-4Al alloy [20]. The chemical composition of Fe-10CR-4Al alloy used in this thesis is reported in Table 2.1.

Table 2.1. Chemical composition of Fe-10Cr-4Al given in weight percentage (wt%).

Alloy	Al	Cr	C	RE	Fe
10-4	4	10	<0.03	Ti, Nb, Zr	Bal.

2.3 Radiation damage

Due to the key role FeCrAl alloys have to play in nuclear applications, these structural materials must sustain not only high temperature, high pressure and aggressive corrosive environment, but also irradiation effects. In fact, neutrons can produce damages in structures and bonds of materials. When neutrons interact with atoms it could lead to their activation, transmutation and displacement damage. It changes the nanostructure of the material causing the production of defects, such as nanocavity, vacancy dislocations loops, self-interstitial atoms (SIA), and SIA dislocation loops. As result of the formation of radiation-induced defect and their interaction with others atoms which lead to the formation of precipitations or more complex combinations of atoms, it occur a change of properties of materials. This phenomenon is enhanced under irradiation and induced if it is not thermodynamically favorable [21].

From a macroscopic point of view, radiation effects depends on the melting temperature of the affected material and the amount of irradiation exposure. It is measured by displacements-per-atom (dpa), that is a unit of absorbed dose in a structural material. Radiation hardening and embrittlement involve all dpa, irradiation creep and swelling involve medium amount of dpa, >10 dpa, while He embrittlement occurs only for an much higher amount of dpa [21].

2.3.1 Radiation hardening

Although hardening mechanism could occur even without irradiation due to the intrinsic presence of defects, radiations enhance the phenomenon by increasing the number of defects. In fact, the presence of defects hampers dislocation motion leading to their deceleration or even a stop with the formation of Orowan loops [22]. As result, an enhancement in yield stress occurs, causing hardening of the material [21].

2.3.2 Radiation embrittlement

The occurrence of radiation embrittlement is correlated with the phenomenon of radiation hardening since both of them are due to same physical origin, such as presence of defects, voids and precipitations. As result a reduction of toughness and ductility is manifested, with an increasing of DBTT [23].

2.3.3 Swelling

It's the transport of matter from the bulk to sinks, resulting in voids and cavities formation. Due to the higher velocity and range of interaction of SIA respect to vacancies, SIA tends to be absorbed at sinks leading to an accumulation of vacancies forming voids in

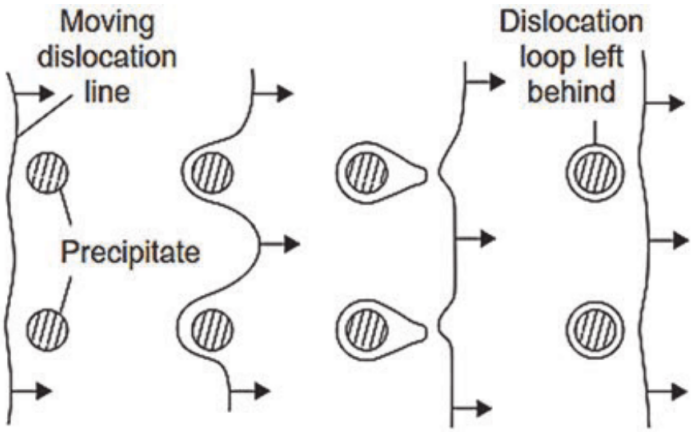

Figure 2.3. Graphical representation of a moving dislocation line forming Orowan loops. Reproduced from *Development of low-cost CrNiMoWMnV ultrahigh-strength steel with high impact toughness for advanced engineering applications.*

the bulk of material. Despite the phenomenon is not expected to occur in LWR due to the lower operating temperature, it is a factor of interest in GEN IV reactors [21] [24].

2.3.4 Proton irradiation

In last years is increasing the amount of evidence encouraging the use of proton irradiation in nuclear materials science to simulate the damage of neutron irradiation to materials. While neutron irradiation require extremely high time and cost to be performed, due the necessity of specialized neutron facilities, proton irradiation could achieve the same dose in shorter time and rapidly provide results. Furthermore, due to the more controllable ion beam energy, dose rate and damage level, sample activation could be avoided, resulting in negligible residual radioactivity, allowing handling of samples. On the other hand, while ion present a very limited penetration depth, neutrons are able to penetrate in a larger scale due to their inherent electrical neutrality [25] [26].

2.4 Liquid metal embrittlement

As mentioned in Section 1.1, the presence of liquid lead as coolant entails many challenges that are currently under research. Among them, the liquid metal embrittlement (LME) represent a significant safety limiting phenomenon in heavy liquid metal cooled nuclear reactors such as LFR and a variant of LFR that uses lead-bismuth eutectic (LBE) as coolant. LME is a phenomenon for which ductile ferritic steels experience drastic loss in tensile ductility or undergo brittle fracture when facing heavy liquid metals as lead and LBE [27]. The mechanisms causing liquid metal embrittlement have not been fully elucidated but typically involves the liquid metal diffusing into the grain boundaries of the solid metal [18]. Once there, it can disrupt the normal bonding between atoms or molecules in the solid metal lattice structure. This disruption weakens the grain

boundaries and reduces the metal's ductility and toughness, making it susceptible to fracture even under relatively low stress. The susceptibility of a metal to liquid metal embrittlement depends on several factors, including the chemical composition of both the solid and liquid metals, the temperature, and the applied stress. The level of oxygen concentration within the molten metal notably affects liquid metal embrittlement. This is because if the metal is capable of creating a protective oxide layer on its surface, the occurrence of LME is prevented due to the absence of direct contact between the solid and liquid phases [18] [28]. Traditionally, it has been observed that ferritic steels are susceptible to liquid metal embrittlement when exposed to lead-bismuth eutectic and lead to some extent. Conversely, austenitic steels have demonstrated lower sensitivity to LME, although they are prone to corrosion and nickel dissolution. Given these observations, it would be reasonable to expect that Fe-10Cr-4Al, like other ferritic steels, would experience LME in low-oxygen environments when in contact with LBE and Pb. However, the study conducted by C. Petersson et al. [18] yielded unexpected results, showing that Fe-10Cr-4Al did not undergo embrittlement in molten lead. This suggests that Fe-10Cr-4Al steel could potentially be utilized as a construction material in Lead Fast Reactors, where it has already demonstrated excellent resistance to corrosion as mentioned in section 2.1.2 [27].

Chapter 3

Methodology

3.1 Slow Strain Rate Testing rig

To study the liquid metal embrittlement phenomenon in stainless steels and test their mechanical properties the Slow Strain Rate Testing (SSRT) rig was developed at KTH. As it is shown in Figure 3.1 the most important components are the precision linear actuator, the load cell, the gas inlet and outlets, the gas-tight vessel, the two-component drawbar, the inert crucible and the U-shaped bracket [18]. The precision linear actuator

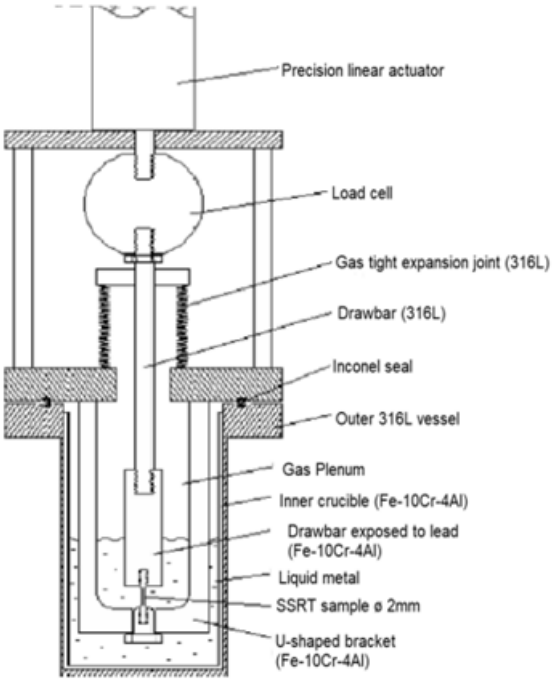

Figure 3.1. SSRT rig.

has a maximum load of 5000 N and a stroke length of 1200 mm, it allows the complete

control of velocity, position torque and applied force. It was thought as an electrical one, instead of an hydraulic or pneumatic one in order to provide higher accuracy and compactness, as well as an easier maintenance and a reduced contaminating risk. The load cell provide measurements to the computer. The gas inlet and outlets allow the insertion of gas into the crucible, providing at the same time the investigation of oxygen conditions, through an oxygen analyzer. The gas-tight vessel is attached to a gas-tight expansion joint that allows the up and down movement of the drawbar, via two two 316L plates with a copper seal in between to ensure no gas leakage. The drawbar is made of two main parts, with the top part connected to actuator, and the bottom part allows the specimen to be screwed into it. While the top part is made of 316L steel, the bottom part is made of Fe-10Cr-4Al alloy to avoid corrosion, since it is designed to be submerged in the liquid lead. Both made of Fe-10Cr-4Al alloy the inner crucible and U-shaped bracket respectively contain the liquid lead and hold the sample in place during tests [18].

3.2 Experimental procedure

As it was said in Section 1.2 this work involves wire testing, resulting in the necessity to adapt the SSRT rig being normally used with samples with M4 threads on both sides and a notch in the middle. As a consequence, three components were developed in collaboration with KTH workshop. The components are shown in Figure 3.2 and Figure 3.3. As upper

Figure 3.2. SSRT adapting tool. Screw used to stretch the wire.

part, to connect the wire to the drawbar, a screw was developed to stretch the wire that is laid through a hole of diameter slightly bigger than 0.2 mm. As bottom part, to hold the wire in place during test, a plate was developed. The wire is passed through the pierced plate and it is fixed by binding it around the cylinder. The wires were around 10 cm long, with a notch in the middle. The aim of notching samples is to obtain deformation and following fracture in a determinate point where irradiation will be performed. The notch effect is to increase the local stress concentration which result in the formation and propagation of cracks. The dimension of the notch was deliberately chosen after comparison test at the same conditions, at is shown in Figure 3.4. The annealed samples were tested at room temperature with different notch size, respectively 100 micron, 80 micron and 60 micron. 60 micron notched samples were not able to perform a proper test,

Figure 3.3. SSRT adapting tools. Plate (right) through which the wire is passed and cylinder (left) around which the wire is bound.

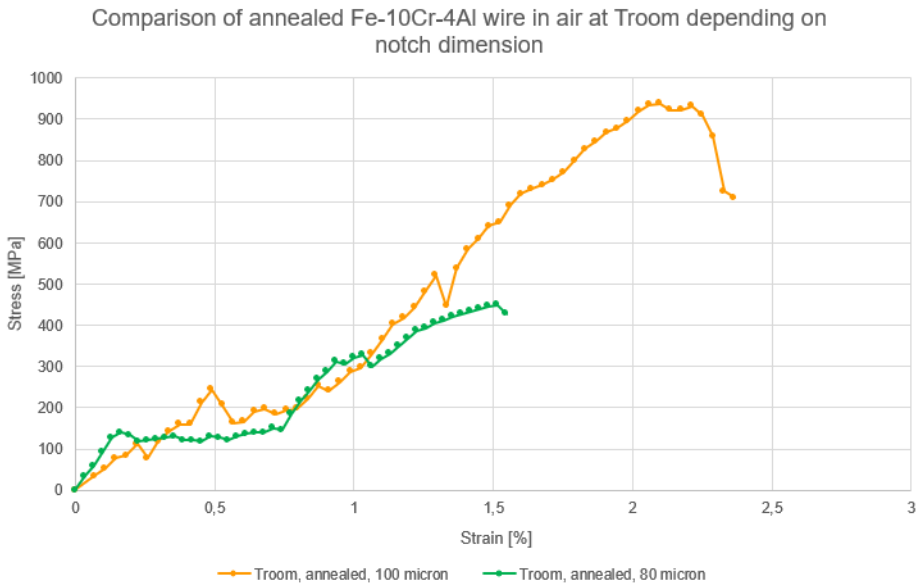

Figure 3.4. Comparison of annealed Fe-10Cr-4Al wire in air at room temperature depending on notch dimension.

resulting in early failures, while both 100 micron and 80 micron notched samples tests resulted in a proper stress-strain curve representation. The deliberately choice to carry on all the following test with a notch of 80 micron was taken due to two main factors: the values of stress-strain were the most similar to the ones obtained in prior studies with the same SSRT rig, resulting in an optimized comparison, and the notch size value represent a good compromise between the minimal size achievable and the predicted implantation depth of ions into Fe-10Cr-4Al sample for a 5.5 MeV ion beam energy, that is the value that will be used for future irradiation campaign.

Before testing, the samples were annealed at $1050°C$ for 45 minutes to avoid almost immediate failure that occurred in micro-sized sampled not annealed. During test, to achieve a low oxygen environment condition the system was flushed with a gas mixture of Ar-5% H2. The oxygen levels stabilized in the SSRT after 3 h. Before the test in lead,

the sample was immersed in the liquid lead at high temperature in low oxygen conditions for almost 24 h. This setting was chosen according to previous experiments with the same SSRT rig on standard sample, to avoid the low wettability between the lead and the steel, in order to ensured good wetting between them and also to to ensure a constant supply of the liquid metal to the crack tip [18]. The strain rate value was deliberately set to $\sim 10^{-5}\ s^{-1}$ and $\sim 10^{-6}\ s^{-1}$, according previous experiments with the same SSRT showing no evident difference in tensile and fracture behaviour. The samples were tested with a slow strain rate testing rig at room temperature, $350°C$, $400°C$ and $450°C$ basing to the values used in previous experiments by C. Petersson et al. [18], in order to achieve good characterization. The tests took between 50 and 120 min, depending on the environmental condition. After the tests in lead, the samples were removed and cleaned with a solution of acetic acid ($C_2H_4O_2$), hydrogen peroxide (H_2O_2) and deionized water in a ratio of 1:1:1, adapting to the microsized samples the ratio 1:1:7 used for previous experiments. The samples were left in the solution for 30 min and then rinsed and dried.

Chapter 4

Results and discussion

4.1 Test results

From SSRT data it is possible to obtain the engineering stress-strain curve. The stress σ is the applied force F over the initial cross section A_0 of the sample as reported in Eq. 4.1.

$$\sigma = \frac{F}{A_0} \tag{4.1}$$

The strain ϵ is the ratio between the sample length variation ΔL over the initial length L_0 of the sample as reported in Eq. 4.2.

$$\epsilon = \frac{\Delta L}{L_0} \tag{4.2}$$

From the engineering stress-strain curve it is possible to observe some remarkable points. The yield strength (YS) point is the stress at which a material begins to deform plastically [29]. It express the limit of elastic behavior and the beginning of plastic behavior. Before YS the material deform elastically and it's able to return to its original shape when the applied stress is removed. After that point, the deformation will be permanent and non-reversible [29]. The ultimate tensile strength (UTS) point is the maximum stress that a material can tolerate before the rupture. In a ductile fracture, it represents the starting of the necking phenomenon for which relatively large amounts of strain localize in a small region of the material, leading to a decrease of local cross-sectional area. A formation of microvoids, their coalescence and the crack propagation at 90° of applied stress is following, until it reach the typical cup and cone fracture [29]. Finally, the fracture point is the stress at which a material fails. In a ductile fracture, the fracture strength is lower than the UTS [30]. Despite for mostly of the tests of this thesis the ultimate tensile strength point and fracture point are similar in terms of MPa, which is generally more common for a brittle fracture, it's evident from fracture surface analysis done with Scanning Electron Microscopy that tests involve a ductile type fracture as seen from the presence of typical ductile structures. The Scanning Electron Microscopy technology will be explained in more detail in Section 4.2. A possible explanation for this phenomenon could be sought in the very small cross section of the sample, leading in a early failure.

4.1.1 Air

The result of test in air at room temperature are shown in Figure 4.1 as an engineering stress-strain curve. The values of yield strength, ultimate tensile strength and total

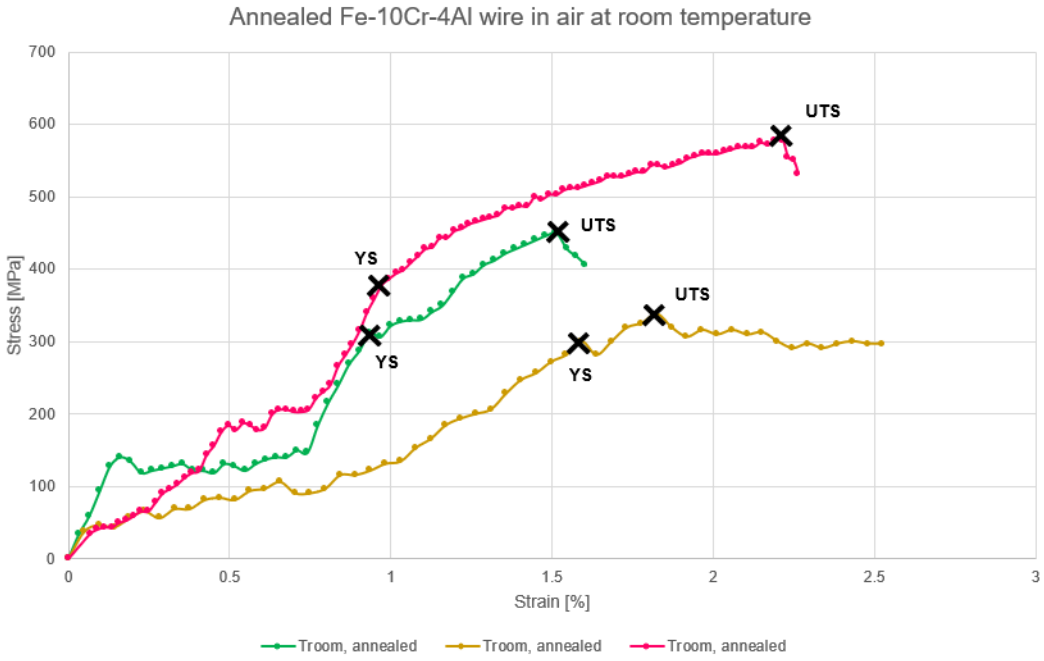

Figure 4.1. 80 micron notched annealed Fe-10Cr-4Al wire in air at room temperature.

elongation to failure are presented in Table 4.1 and compared with values from Fe-10Cr-4Al standard samples tested in air at room temperature from previous experiments. It's shown an averaged reduction of the yield strength of 24% and an averaged reduction of the ultimate tensile strength of 19%. While the yield strength and ultimate tensile strength shows a comparable reduction in terms of MPa, the total elongation to failure shows an enormous reduction, with an averaged diminution of 97%. This trend is expected as the microsized samples shows a comparable mechanical response in terms of limit of elastic behaviour and the maximum stress that the sample can tolerate before the rupture. On the other hand, the total elongation to failure is significantly lower due to lower cross section of the wire, leading to a faster necking phenomenon and an early rupture. Thus, it is not possible to define a clear YS point, due to the fact the transition between elastic and plastic behaviour is not well-defined. Despite this, the slope of the engineering stress-strain curve has been analysed and the points where the trend of the curves flatten out more have been chosen as YS points.

Figure 4.2 shows the comparison between the stress-strain behaviour of micro-sized sample and the classic one. As it was said before, the difference is well expected, due to

Table 4.1. Comparison of yield strength, ultimate tensile strength and total elongation to failure data of samples tested in air at room temperature.

T [°C]	Condition	YS [MPa]	UTS [MPa]	Total elongation to failure [%]	Sample type	Ref
Troom	air	454	561	25.0	Classic	[18]
Troom	air	441	547	24.97	Classic	[18]
Troom	air	436	542	30.0	Classic	[18]
Troom	air	389	541	2.2	Wire	
Troom	air	301	451	2.6	Wire	
Troom	air	311	339	1.6	Wire	

the massive difference in term of cross section.

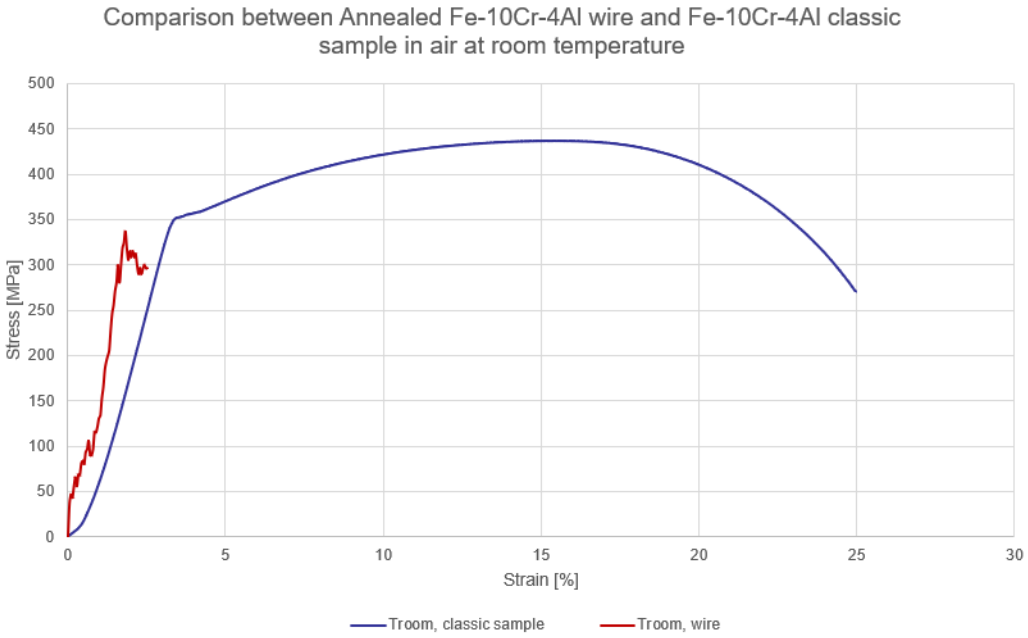

Figure 4.2. Comparison between Annealed Fe-10Cr-4Al wire and Fe-10Cr-4Al classic sample in air at room temperature.

4.1.2 Ar-5% H2

The result of test in Ar-5% H2 are shown in Figure 4.3, Figure 4.4 and Figure 4.5 as an engineering stress- strain curve, respectively reporting test results at 350°C, 400°C and 450°C. While for 350°C and 400°C test it is still possible to define yield strength point, although not as clearly as the test in air, for the higher temperature test it is not possible, due to the lack of consistency between tests and a not well-defined transition point between elastic and plastic behaviour. The values of yield strength, ultimate tensile

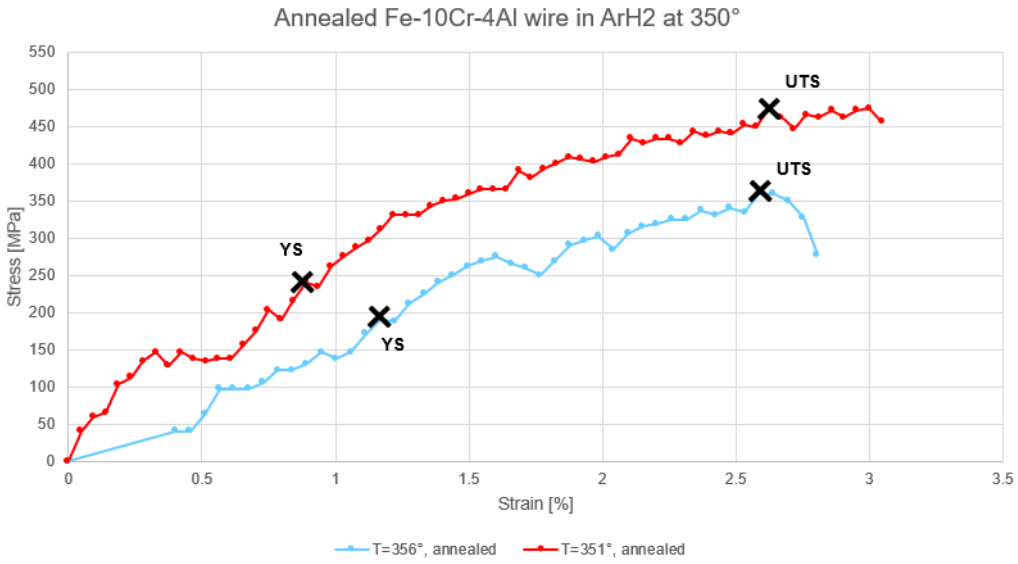

Figure 4.3. 80 micron notched annealed Fe-10Cr-4Al wire in Ar-5% H2 at 350°C.

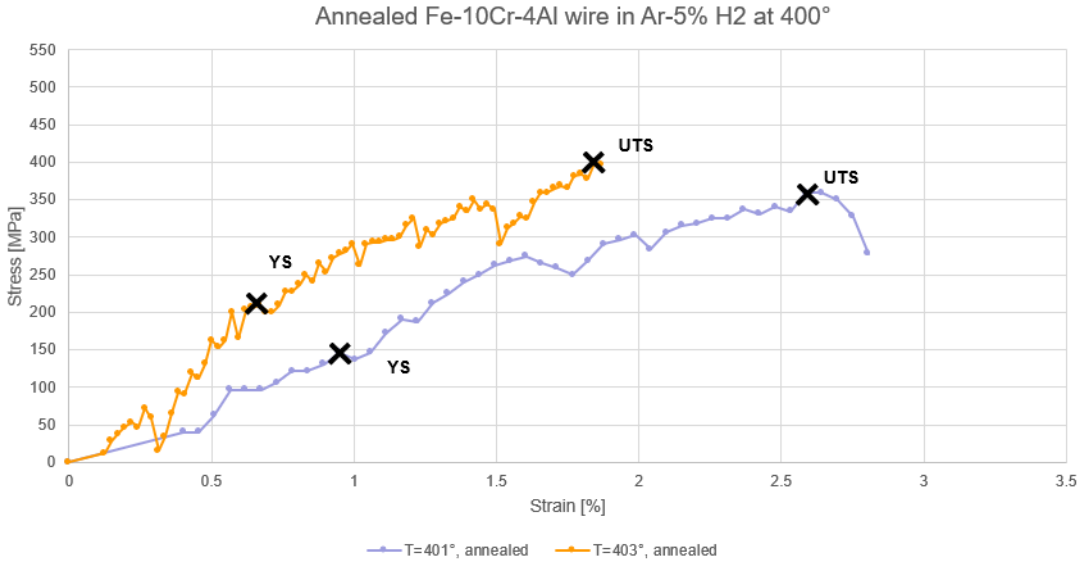

Figure 4.4. 80 micron notched annealed Fe-10Cr-4Al wire in Ar-5% H2 at 400°C.

strength and total elongation to failure are presented in Table 4.2 and compared with values from Fe-10Cr-4Al standard samples tested in Ar-5% H2 from previous experiments [18]. Comparing test results with the ones already present in literature at the same temperature, it is possible to observe an averaged reduction of the yield strength of 35% and an averaged reduction of the ultimate tensile strength of 21% for test carried

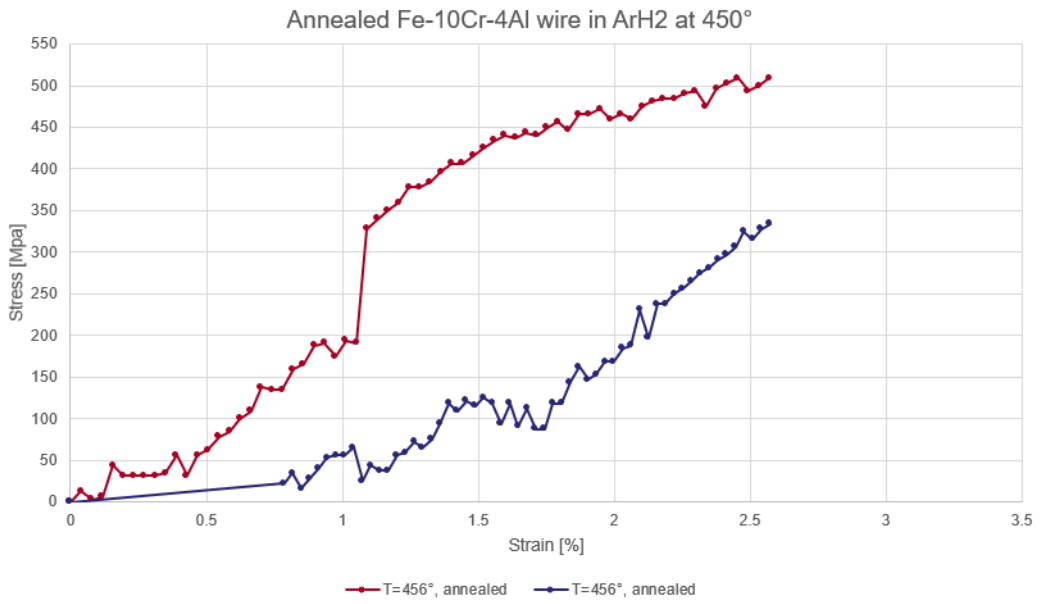

Figure 4.5. 80 micron notched annealed Fe-10Cr-4Al wire in Ar-5% H2 at 450°C.

out at similar temperature around 350°C. While the total elongation to failure at that temperature shows a reduction of 86% [18]. Comparing the results from literature, it occurs an averaged decrease in yield strength between air and Ar-5% H2 of 16%, slightly bigger than the averaged decrease in yield strength between values obtained in this work, which result of 3%. For what concerned the decrease in ultimate tensile strength between air and Ar-5% H2, the results are more comparable between literature and this thesis since they are respectively 8% and 6% [18]. The reduction in UTS and YS it is expected, since it is due to the increased temperature causing the softening of the material, while the percentile difference of the reduction is due to the difficulty to define a proper YS point for the wire stress-strain curve.

Table 4.2. Comparison of yield strength, ultimate tensile strength and total elongation to failure data of samples tested in Ar-5% H2 at 350°C and 400°C.

T [°C]	Condition	YS [MPa]	UTS [MPa]	Total elongation to failure [%]	Sample type	Ref
350	Ar-5% H2	384	511	20.5	Classic	[18]
370	Ar-5% H2	371	508	18.0	Classic	[18]
351	Ar-5% H2	248	456	3.1	Wire	
356	Ar-5% H2	222	361	2.7	Wire	
403	Ar-5% H2	202	402	1.7	Wire	
401	Ar-5% H2	148	352	2.7	Wire	

4.1.3 Liquid Pb

The result of test in liquid Pb are shown in Figure 4.6, Figure 4.7 and Figure 4.8 as an engineering stress-strain curve, respectively reporting test results at $350°C$, $400°C$ and $450°C$. Liquid lead tests shows the same particular pattern shown by test in Ar-5% H2.

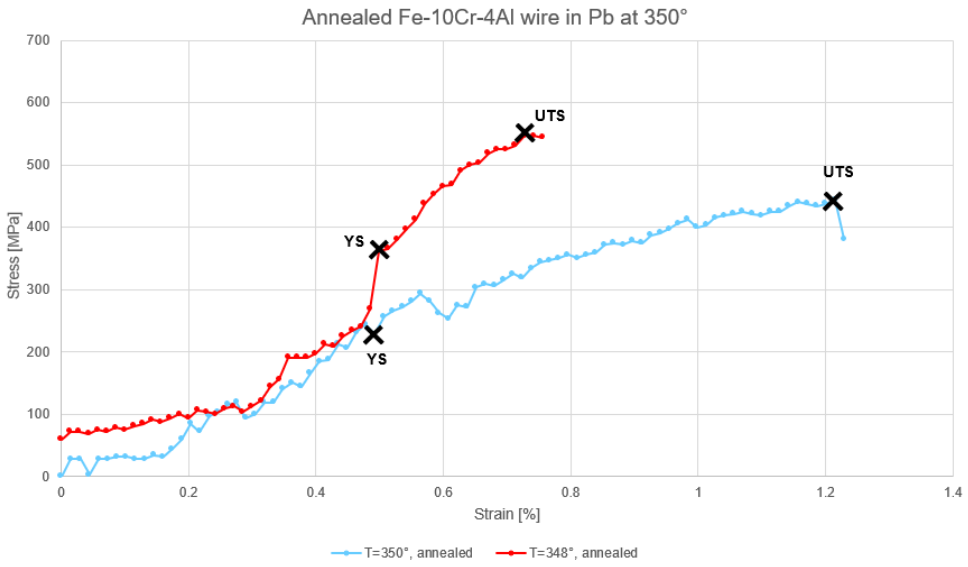

Figure 4.6. 80 micron notched annealed Fe-10Cr-4Al wire in liquid lead at $350°C$.

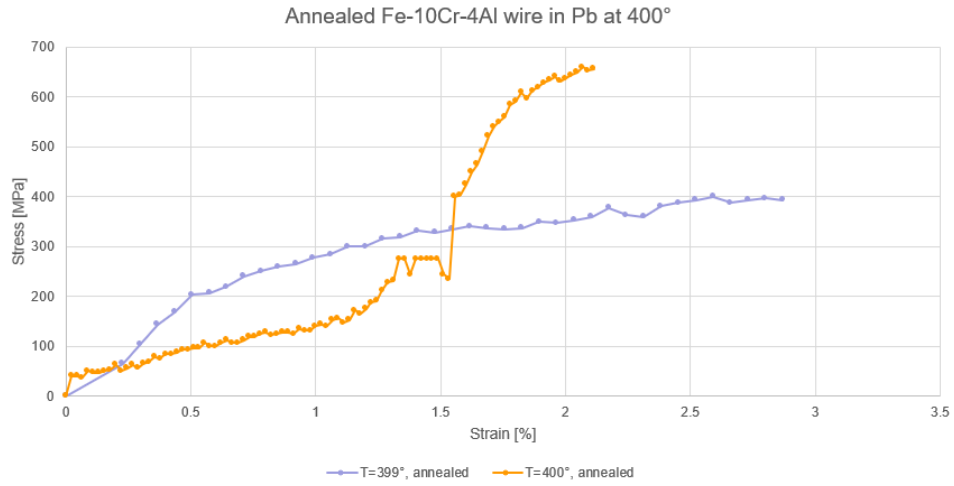

Figure 4.7. 80 micron notched annealed Fe-10Cr-4Al wire in liquid lead at $400°C$.

While for $350°C$ test it is still possible to define a sort of yield strength point, however not as clearly as before, and the slope of tests carried out shows a kind of consistency, for

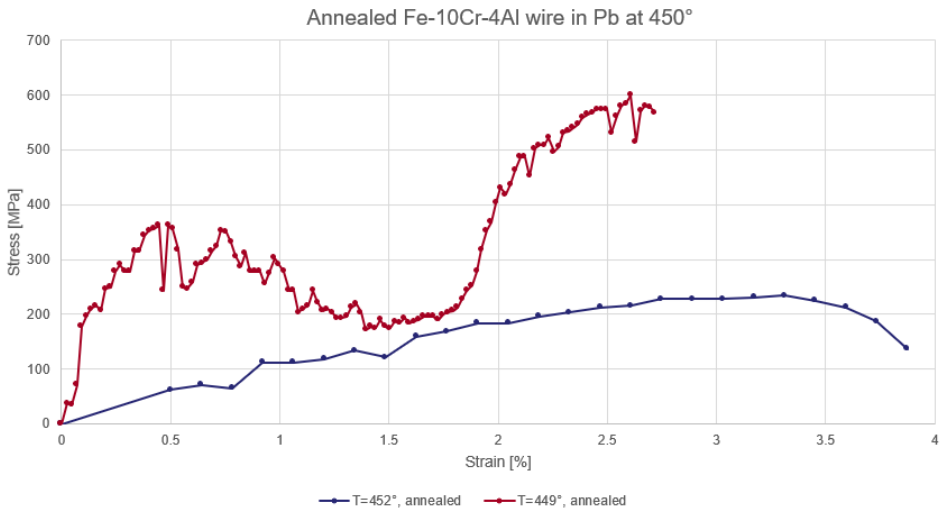

Figure 4.8. 80 micron notched annealed Fe-10Cr-4Al wire in liquid lead at 450°C.

the higher temperature test it is not possible, due to the lack of a regular pattern between tests and a not well-defined transition point between elastic and plastic behaviour. While study carried out by C. Petersson et al. [18] indicates that the strain at rupture is non dependant on the temperature of the liquid lead, the tests presented in this work show an increase of strain at rupture as temperature arise [18]. More tests have to be performed in order to investigate this phenomenon.
The values of yield strength, ultimate tensile strength and total elongation to failure are presented in Table 4.3 and compared with values from Fe-10Cr-4Al standard samples tested in liquid lead from previous experiments [18].

Table 4.3. Comparison of yield strength, ultimate tensile strength and total elongation to failure data of samples tested in liquid lead at 350°C.

T [°C]	Condition	YS [MPa]	UTS [MPa]	Total elongation to failure [%]	Sample type	Ref
340	liquid Pb	388	540	25.0	Classic	[18]
350	liquid Pb	390	534	24.9	Classic	[18]
350	liquid Pb	398	516	21.0	Classic	[18]
358	liquid Pb	379	517	24.8	Classic	[18]
372	liquid Pb	389	531	24.97	Classic	[18]
348	liquid Pb	382	553	0.7	Wire	
350	liquid Pb	256	461	1.2	Wire	

Comparing test results with the ones already present in literature at the same temperature in the lead environment, it is possible to observe an averaged reduction of the yield

strength of 18% and an averaged reduction of the ultimate tensile strength of 4% for test carried out at similar temperature around 350°C in liquid lead. While the total elongation to failure at that temperature shows a reduction of 96% [18]. In the Figure

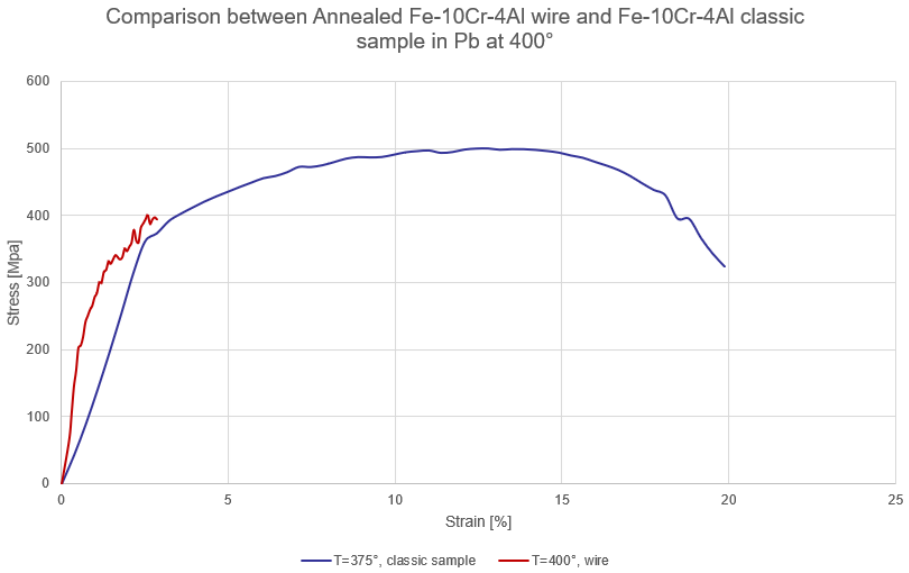

Figure 4.9. Comparison between Annealed Fe-10Cr-4Al wire and Fe-10Cr-4Al classic sample in liquid lead at 400°.

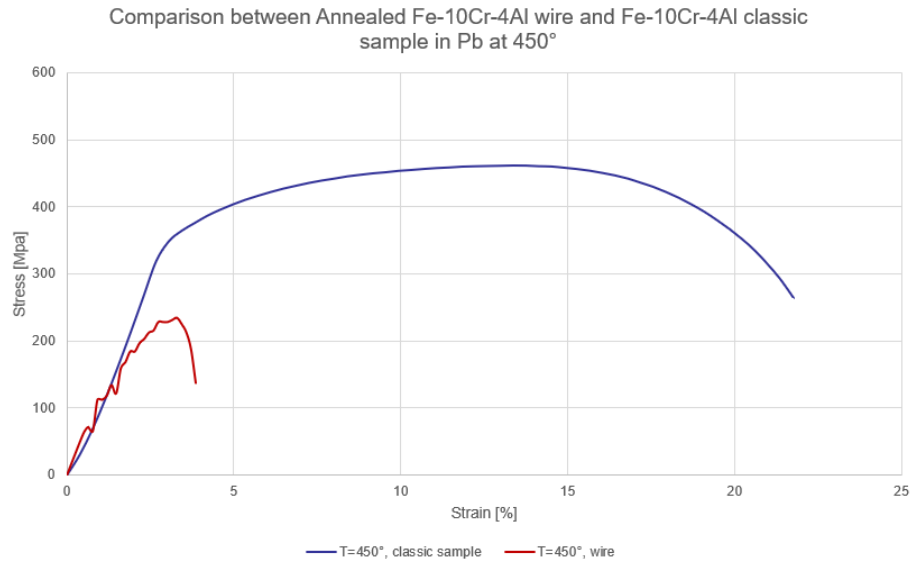

Figure 4.10. Comparison between Annealed Fe-10Cr-4Al wire and Fe-10Cr-4Al classic sample in Pb at 450°.

4.9 and Figure 4.10 it is showed the comparison between the stress-strain behaviour of micro-sized sample and the classic one in liquid lead. Figure 4.9 shows the comparison at $400°C$, while Figure 4.10 shows the comparison at $450°C$. As it was for room temperature and air environment, the difference is well expected, due to the massive difference in term of cross section.

4.2 Fracture surface analysis

The analysis of the fracture surface is carried out with the Scanning Electron Microscopy (SEM) technology, that is able to generate images of the sample by scanning the surface with a focused beam of electrons. The interaction between electrons and atoms of sample generate signals which intensity depends on surface topography and composition. The position of the beam combined with the intensity of the signal produce an image [31].

The images obtained with SEM of sample tested in lead at $449°C$ are shown in Figure 4.11. Due to the relatively small fracture area a definite evaluation can't be achieved, but

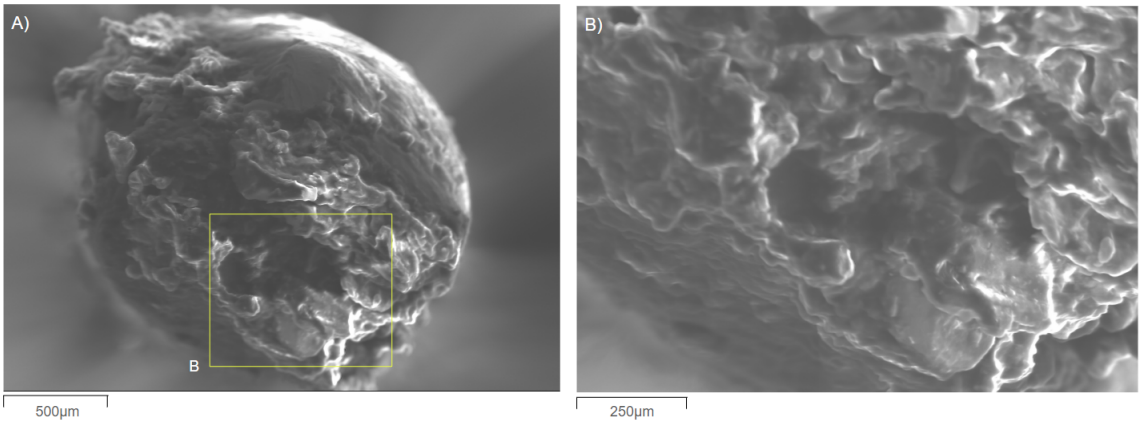

Figure 4.11. A) SEM image of the fracture surface of sample tested in liquid lead at $449°C$. B) Zoom of ridges of A.

it can be observed a sort of cup and cone fracture that indicate mode I ductile fracture with dimples in the center of the sample. This type of fracture occurs in ductile materials subjected to uniaxial force and it is caused by void nucleation and coalescence which lead to crack growth and failure [32] [33]. Figure 4.11B shows a valley structure in the middle with ridges in the edges which is typical for this type of failure. Then sample shows a mixture of intergranular crack propagation, for which the failure propagates along grain boundaries, and transgranular crack propagation, for which the crack propagates through the grains, with a predominance of the second one. The small area does not allow to appreciate dimple formation in the middle, but their presence is a reasonable assumption. Since that images don't seem to show any brittle fracture mode in the middle, that could be the indication of the absence of LME, but a clear answer is hard to give. This is mainly due to complexity of the phenomenon at its dependence on many factor as temperature, applied load, grain size, oxygen concentration and material composition. On the edges

are present some lead leftovers that were not removed from the sample surface by the acetic acid, hydrogen peroxide and deionized water solution.
Figure 4.12 shows the overview of sample tested in lead at $367°C$, and ductile failure structure with dimple formation could be seen in the centre of the sample, that could be a sign of the fact that LME is not present (4.12C and D). However, as it is shown in

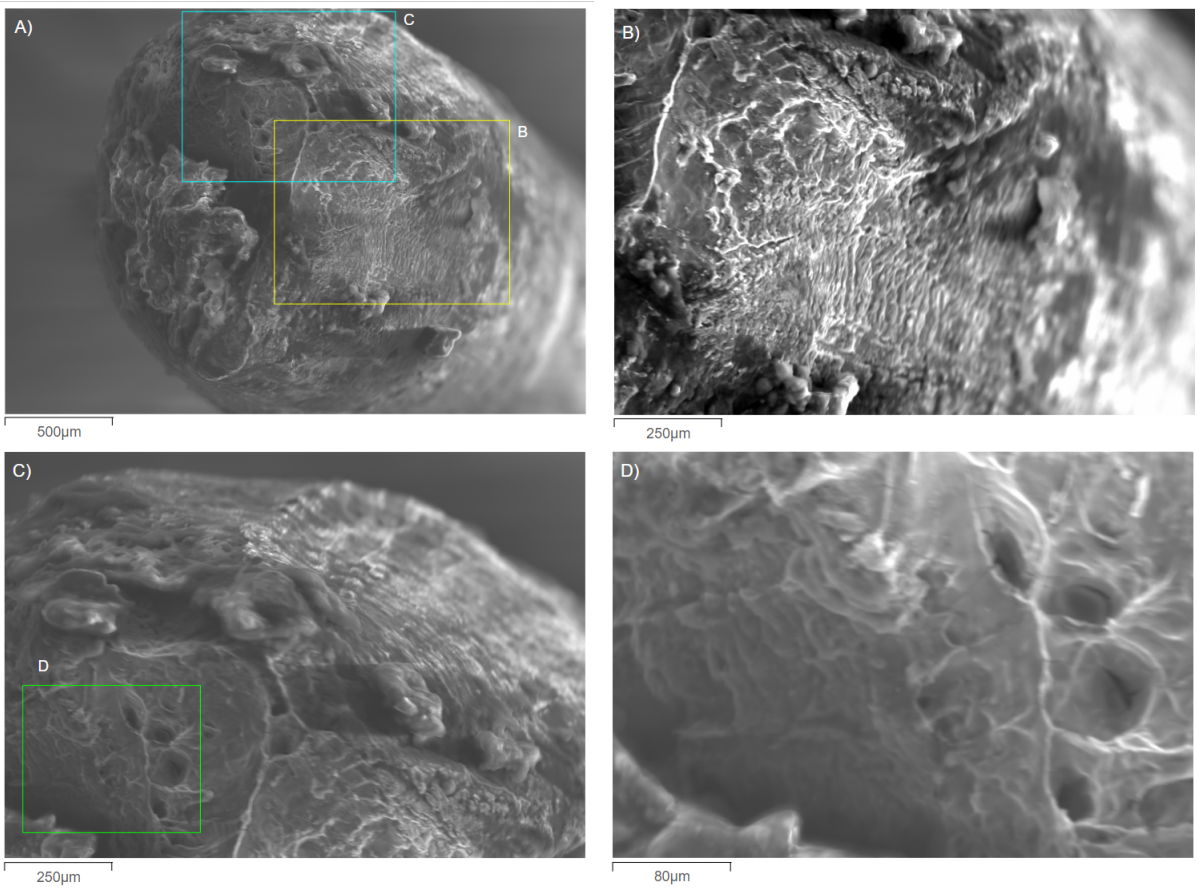

Figure 4.12. A) SEM image of the fracture surface of sample tested in liquid lead at $367°C$. B) Zoom of edge of A. C) Zoom of the centre of A. and D) Zooms of a detail of C.

Figure 4.12B on the edge, in the right part of the image the granular structures commonly present in a brittle fracture are present. It's common not to have a fully ductile or brittle failure, so a mix of ductile and brittle structures and composition is well expected on the edges [32].

The sample surface composition was investigated using energy dispersion spectroscopy (EDS) analyzer in the SEM. It is an analytical technique used for the chemical characterization of the sample. The interaction between the X-ray and the sample lead to the formation of unique set of peaks on the electromagnetic emission spectrum, due to the fact each element has a unique atomic structure, resulting in a different peaks [34].

As it is shown in Figure 4.13, after the exposure, small concentration of alumina oxide could be detected on the sample surfaces. The protective alumina oxide acts as an improvement in corrosion resistance, helping to avoid liquid metal embrittlement. This could be considered a further sign of the not occurrence of LME.

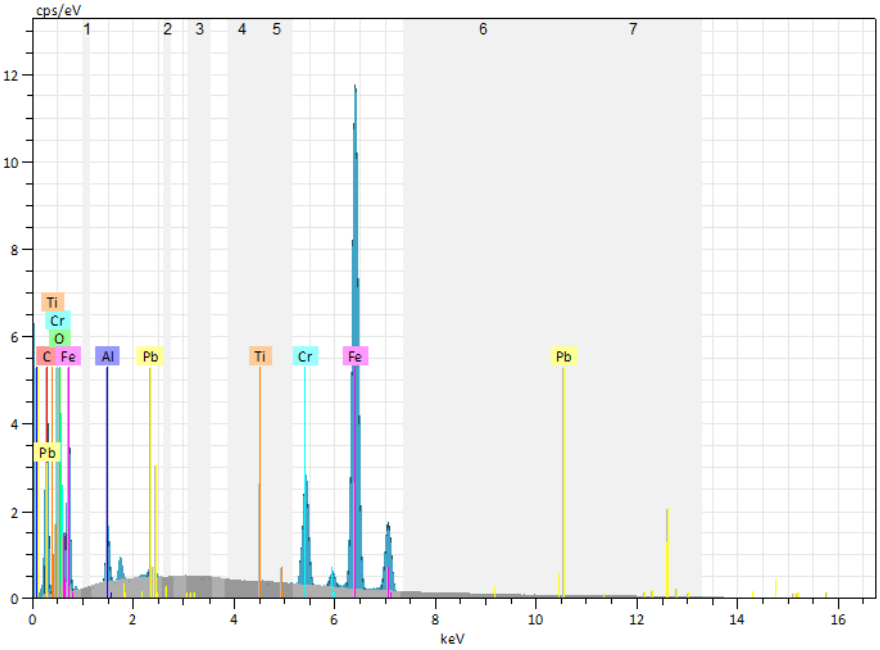

Figure 4.13. EDS spectrum of the Fe-10Cr-Al sample surface.

The surface composition of the sample investigated by the energy dispersion spectroscopy analyzer is reported in Table 4.4.

Table 4.4. The chemical surface composition of the sample given in weight percentage (wt%).

Element	Series	C Atom. [wt.%]	C [at.%]
Carbon	K-series	13.85	40.65
Oxygen	K-series	2.23	4.92
Aluminium	K-series	2.33	3.05
Chromium	K-series	7.42	5.035
Iron	K-series	73.09	46.14
Lead	M-series	1.04	0.18
Titanium	K-series	0.03	0.02

The images obtained with SEM of sample tested in Ar-5% H2 at $456°C$ are shown in 4.14. It could be appreciated a sort of neck formation, with similar consideration as the previous lead samples. While it seems showing dimples formation in the middle of the sample, the edges are more unclear, with a mix of ductile and brittle fracture structure.

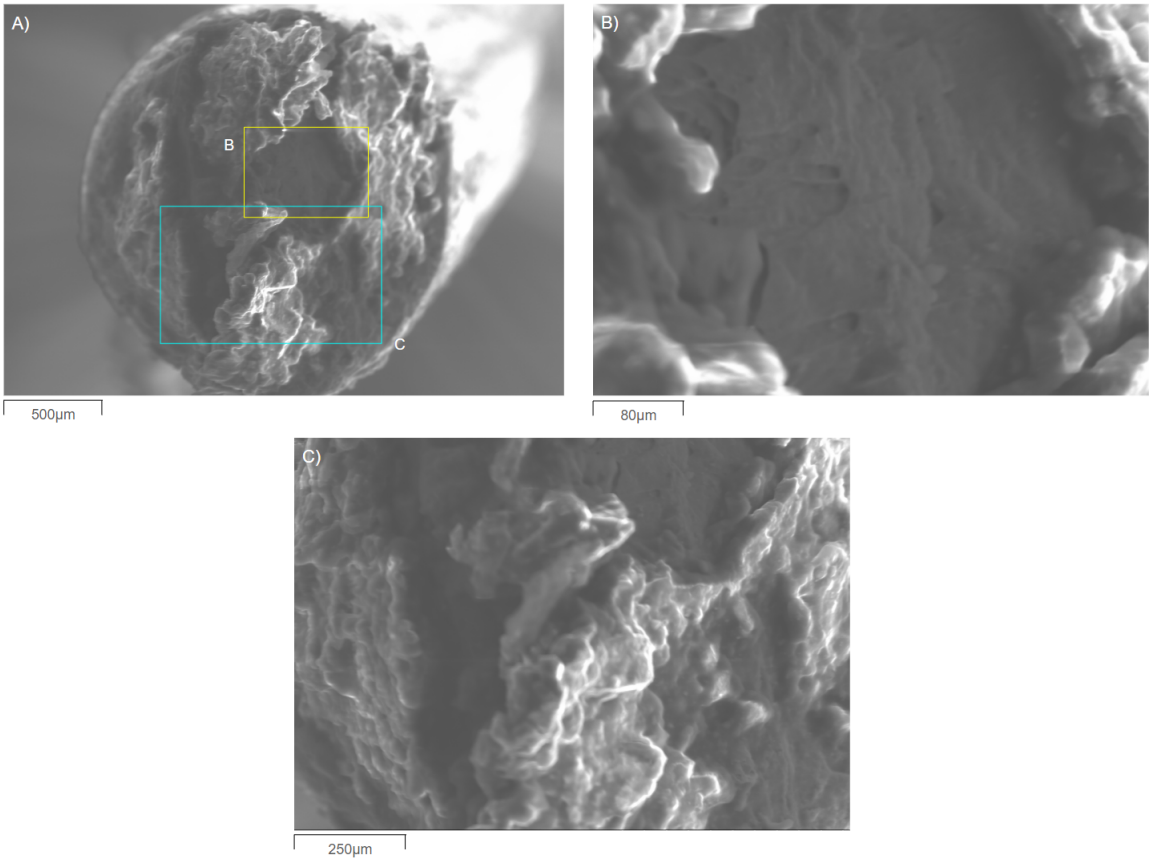

Figure 4.14. A)SEM image of the fracture surface of sample tested in Ar-5% H2 at 456°C, B) Zoom of a detail of A. C) Zoom of ridges and valley of A.

The SEM images obtained with the test in air at room temperature show the same pattern of Ar-5% H2 images.

Chapter 5

Conclusion

The Fe-10Cr-4Al samples were tested with a slow strain rate testing rig at room temperature, $250°C$, $350°C$, $400°C$ and $450°C$ in air, in a gas mixture of Ar-5% H2 and in liquid lead. This choice of temperature and environment was based on Fe-10Cr-4Al previous experiments with the same SSRT rig on standard samples, in order to achieve higher characterization. The results showed that FeCrAl micro-sample mechanical representation could be compared to standard samples values already present in literature for what concerned room temperature and air experiments, with a slight decrease in yield strength and ultimate tensile strength and at the same time, a massive reduction in terms of total elongation to failure. The values obtained reflect what it was expected. A similar pattern was achieved for Ar-5 % H2 and liquid lead at $350°C$, while higher temperature test showed lack of consistency. Further experiments will help to ensure higher characterization to define a clearly mechanical response, in order to define yield strength and ultimate tensile strength values to compare to ones already present in literature.

From the obtained results, no sign of LME occurrence seems to have been found since the SEM images do not show brittle structures in the middle of the samples which would be likely to occur in case of LME. However, it should be considered that the evaluation of the obtained results involves big uncertainties and it doesn't allow to have clear answers for Fe-10Cr-4Al response to LME.

5.1 Future work

Because high temperature test showed lack of consistency and the number of tests that were carried out were not enough to have proper characterization, an additional amount of experiments in same conditions would be beneficial. In addiction, more test with different diameter size of micro-sized sample would help to understand the feasibility of minimal dimension intuition to achieve a comparable mechanical response to the standard metallic behaviour. Further fracture surface analysis with an higher resolution SEM would be necessary to investigate with greater precision the edges of the sample and the central part to evaluate the presence of dimples and to define clearly the not occurrence of LME.

Finally, an irradiation process would be necessary to evaluate changes in terms of mechanical properties such as total elongation to failure and fracture elongation and to

proper analyse of irradiation acts on liquid metal embrittlement phenomenon. If results would look promising a further investigation with neutron irradiation would improve the evaluation of irradiated Fe-10Cr-4Al in a real reactor environment.

Bibliography

[1] Hannah Ritchie and Pablo Rosado. Fossil fuels. *Our World in Data*, 2017. https://ourworldindata.org/fossil-fuels.

[2] Hannah Ritchie. What are the safest and cleanest sources of energy? *Our World in Data*, 2020. https://ourworldindata.org/safest-sources-of-energy.

[3] Scott Miller, G.; Spoolman. Environmental science: Problems, connections and solutions. *Cengage Learning*, 2018.

[4] Generation iv nuclear reactors. *World Nuclear Association*, 2020. https://world-nuclear.org/information-library/nuclear-fuel-cycle/nuclear-power-reactors/generation-iv-nuclear-reactors.aspx.

[5] Generation iv international forum. gen iv reactor design. *The Generation IV International Forum*, 2013. https://www.gen-4.org/gif/jcms/$c_4$0275/$gen- \ iv \ -reactor \ - \ design$.

[6] Generation iv international forum. generation iv goals. *The Generation IV International Forum*. https://www.gen-4.org/gif/jcms/$c_9$502/$generation - iv - goals$.

[7] Mauro Mancini Giorgio Locatelli and Nicola Todeschini. Generation iv nuclear reactors: Current status and future prospects. *Energy Policy*, 61:1503–1520, 2013. https://www.sciencedirect.com/science/article/pii/S0301421513006083.

[8] Lead-cooled fast reactor. *The Generation IV International Forum*. https://www.gen-4.org/gif/jcms/$c_4$2149/$lead - cooled - fast - reactor - lfr$.

[9] M. Takahashi T. Obara M. Kondo A. Moiseev L. Tocheny C. Smith I. S. Hwang Y. Wu M. Jin A. Alemberti, K. TuÄek. Lead-cooled fast reactor (lfr) system safety assessment. 2020. https://www.gen-4.org/gif/upload/docs/application/pdf/2020-06/gif$_l fr_s sa_j une_2 020_2 020 - 06 - 09_1 7 - 26 - 41_2 02.pdf$.

[10] Snead Mary A. Yamamoto Yukinori Field, Kevin G. and Kurt A. Terrani. Handbook on the material properties of fecral alloys for nuclear power production applications. 2018. https://www.osti.gov/biblio/1474581.

[11] Jun Lim, Il Soon Hwang, and Ji Hyun Kim. Design of alumina forming fecral steels for lead or leadâbismuth cooled fast reactors. *Journal of Nuclear Materials*, 441(1):650–660, 2013. https://www.sciencedirect.com/science/article/pii/S0022311512001778.

[12] Geelhood K.E. Goodson, Carole E. Degradation and failure phenomena of accident tolerant fuel concepts. 2020. https://www.nrc.gov/docs/ML2027/ML20272A218.

[13] Y.-J. Kim K.A. Unocic Y. Yang C.M. Silva H.M. Meyer III R.B. Rebak K.A. Terrani, B.A. Pint. Uniform corrosion of fecral alloys in lwr coolant environments. 2016. https://www.sciencedirect.com/science/article/abs/pii/S0022311516303014aep-article-footnote-id20.

[14] Yin Ling Rebak, Raul B. Resistance of ferritic fecral alloys to stress corrosion cracking for light water reactor fuel cladding aplications. 2020. https://doi.org/10.5006/3632.

[15] Briggs Samuel A. Hu Xunxiang Yamamoto Yukinori Howard Richard H. Sridharan Kumar Field, Kevin G. Heterogeneous dislocation loop formation near grain boundaries in a neutron-irradiated commercial fecral alloy. 2016. https://doi.org/10.1016/j.jnucmat.2016.10.050.

[16] J. Stringer F. H. Stott, G. C. Wood. The influence of alloying elements on the development and maintenance of protective scales. 1995. https://link.springer.com/article/10.1007/BF01046725.

[17] W. Chubb, S. Alfant, A. A. Bauer, E. J. Jablonowski, F. R. Shober, and R. F. Dickerson. Constitution, metallurgy, and oxidation resistance of iron-chromium- aluminum alloys. https://www.osti.gov/biblio/4290548.

[18] Szakalos Peter Petersson, Christopher and Daniel Dietrich Stein. Slow strain rate testing of fe-10cr-4al ferritic steel in liquid lead and leadâbismuth eutectic s. 2023. https://doi.org/10.1016/j.nme.2023.101403.

[19] Jesper Ejenstam and Peter Szakalos. Long term corrosion resistance of alumina forming austenitic stainless steels in liquid lead. *Journal of Nuclear Materials*, 461:164–170, 2015. https://www.sciencedirect.com/science/article/pii/S0022311515001555.

[20] Szakalos Peter Domstedt, Peter and Jesper Ejenstam. High temperature corrosion of a lean alloyed fecral-steel and the effects of impurities in liquid lead. 2020. 10.1109/EEE-IC/ICPSEurope49358.2020.9160504.

[21] Andrea E. Sand Fredric Granberg Robert S. Averback Roger E. Stoller Tomoaki Suzudo Lorenzo Malerba Florian Banhart William J. Weber Francois Willaime Sergei L. Dudarev David Simeone Kai Nordlund, Steven J. Zinkle. Primary radiation damage: A review of current understanding and models. 2018. https://doi.org/10.1016/j.jnucmat.2018.10.027.

[22] Mohammed Ali. Development of low-cost crnimowmnv ultrahigh-strength steel with high impact toughness for advanced engineering applications. 08 2020. https://www.researchgate.net/publication/343850877.

[23] M S Wechsler. Radiation embrittlement of metals and alloys. https://www.osti.gov/biblio/4109831.

[24] Edward A. Little and David Stow. Void-swelling in irons and ferritic steels: Ii. an experimental survey of materials irradiated in a fast reactor. *Journal of Nuclear Materials*, 87:25–39, 1979. https://api.semanticscholar.org/CorpusID:93071149.

[25] *Simulation of Neutron Irradiation Effects with Ions*, pages 545–577. Springer Berlin Heidelberg, Berlin, Heidelberg, 2007. https://doi.org/10.1007/978-3-540-49472-$0_1$1.

[26] G.S Was, J.T Busby, T Allen, E.A Kenik, A Jensson, S.M Bruemmer, J Gan, A.D Edwards, P.M Scott, and P.L Andreson. Emulation of neutron irradiation effects with protons: validation of principle. *Journal of Nuclear Materials*, 300(2):198–216, 2002. https://www.sciencedirect.com/science/article/pii/S0022311501007516.

[27] Joseph, B., Picat, M., and Barbier, F. Liquid metal embrittlement: A state-of-the-art appraisal. *Eur. Phys. J. AP*, 5(1):19–31, 1999. https://doi.org/10.1051/epjap:1999108.

[28] Ingrid Proriol Serre and Jean-Bernard Vogt. Liquid metal embrittlement sensitivity of the t91 steel in lead, in bismuth and in lead-bismuth eutectic. *Journal of Nuclear Materials*, 531:152021, 2020. https://www.sciencedirect.com/science/article/pii/S0022311519315284.

[29] Elfetori F. Abdewi. Mechanical properties of reinforcing steel rods produced by zliten steel factory. In *Reference Module in Materials Science and Materials Engineering*. Elsevier, 2017. https://www.sciencedirect.com/science/article/pii/B9780128035818103625.

[30] E.P. DeGarmo, E.P. DeGarmo, J.T. Black, and R.A. Kohser. *Materials and Processes in Manufacturing*. Number v. 1 in Materials and Processes in Manufacturing. Wiley, 2003. https://books.google.it/books?id=DdMmAQAAMAAJ.

[31] Sandy Burany. Scanning electron microscopy and x-ray microanalysis. j. goldstein, d. newbury, d. joy, c, lyman, p. echlin, e. lifshin, l. sawyer, and j. michael. kluwer academic, plenum publishers, new york; 2003, 688 pages (hardback, 75.00)$isbn0 - 306 - 47292 - 9. Microscopy and Microanalysis - MICROSCMICROANAL, 9 : 484 - -484, 102003. 10.1017/S1431927603030617$.

[32] Wenxuan Tang, X. C. Tang (Xiaochang Tang), Yonghui Mo, Lingyi Meng, and Xiaohu Yao. Cup-cone structure analysis: A novel statistical approach to evaluate the structure-performance relationship of metallic glasses. *SSRN Electronic Journal*, 01 2022. 10.2139/ssrn.4266839.

[33] Kevin G. Field, Samuel A. Briggs, Ken Littrell, Chad M. Parish, and Yukinori Yamamoto. Database on performance of neutron irradiated fecral alloys. https://www.osti.gov/biblio/1295144.

[34] G Lawes. Scanning electron microscopy and x-ray microanalysis. https://www.osti.gov/biblio/5023989.